Evolution of the subglacial drainage system beneath the Greenland Ice Sheet revealed by tracers

Chandler, D. M.; Wadham, J. L.; Lis, G. P.; Cowton, T.; Sole, A.; Bartholomew, I.; Telling, J.; Nienow, P.; Bagshaw, E. B.; Mair, D.; Vinen, S.; Hubbard, A.

Published in:
Nature Geoscience

DOI:
10.1038/ngeo1737

Publication date:
2013

Citation for published version (APA):
Chandler, D. M., Wadham, J. L., Lis, G. P., Cowton, T., Sole, A., Bartholomew, I., Telling, J., Nienow, P., Bagshaw, E. B., Mair, D., Vinen, S., & Hubbard, A. (2013). Evolution of the subglacial drainage system beneath the Greenland Ice Sheet revealed by tracers. *Nature Geoscience*, *6*(3), 195-198. https://doi.org/10.1038/ngeo1737

nature geoscience

SUPPLEMENTARY INFORMATION

DOI: 10.1038/NGEO1737

Evolution of the subglacial drainage system beneath Greenland's ice sheet revealed by tracers

D.M. Chandler, J.L. Wadham, G.P. Lis, T. Cowton, A. Sole, I. Bartholomew, J. Telling, P. Nienow, E.B. Bagshaw, D. Mair, S. Vinen and A. Hubbard

S1. TRACER INJECTION AND MEASUREMENT

Rhodamine dye was injected directly into streams draining into the moulins. With the exception of Site L7 traces in June 2011, SF_6 was injected down 150 m of 12 mm internal diameter hose arranged with one end in the moulin and the other fixed at the surface. The mass of gas injected was controlled by passing the gas through a pre-calibrated flow meter at a controlled rate (typically 15 litres per minute) for a known time. In June 2011, traces at Site L7 were injected by pre-saturating a 2000-litre inflatable water tank over a period of ~3 hours; the tank was then drained via a 25 mm internal diameter hose with its lower end several metres below the moulin water level. Assuming the tank was approximately 75% full (1500 litres), then an assumed SF_6 saturation level of 74 mg/litre at 0°C[1] sets an upper limit on the amount injected at 110 g. In June 2011, the moulin water level was measured using a Bosch Sensortec BMD040 absolute pressure sensor potted in aluminium tubing and logged at the surface with a Campbell Scientific CR10X data logger. Relative to the ice surface, water levels during injections were at +0.1 m (13 June), +0.2 m (15 June), -10.2 m (17 June) and -37.5 m (19 June). The moulin formed as a crack on 7 June, which rapidly drained the water-filled channels above and then overflowed each afternoon up to and including 15 June.

Dye concentrations were monitored in the single river emerging from the terminus of Leverett Glacier. River water fluorescence was measured in-situ approximately 700 m downstream from the glacier terminus using a Turner Designs Cyclops fluorometer and Campbell Scientific data logger (model CR10X or CR1000) at 1-minute intervals. The Cyclops fluorometer outputs a voltage that varies linearly with dye concentration over its specified range (0.01 to 1000 ppb: Turner Designs[2]). Fluorometer output was therefore converted to dye concentration using a linear calibration obtained by successive dilutions of a standard solution (Fig. S1.1). This technique has been widely used in previous hydrological studies of Alpine and Arctic valley glaciers[3-6].

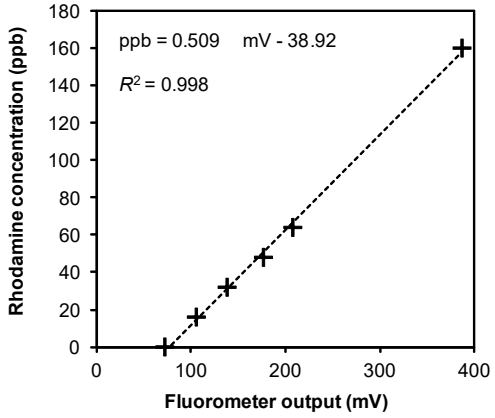

Figure S1.1: *A typical calibration used to convert fluorometer signal (mV) to dye concentration (ppb).Calibrations yielded R^2 values better than 0.99.*

River water samples intended for SF_6 analysis in the field were collected from the same site as the fluorometer, in 50 ml glass gas-tight syringes which were rinsed 3 times with river water prior to filling with the river water sample. Care was taken to ensure no air bubbles were present in the samples. Syringes were sealed using a 3-way valve. Prior to analysis, a 20 ml headspace was created in the syringe by adding 100% N_2 gas at atmospheric pressure; the syringe was then shaken to equilibrate the SF_6 between the water and headspace.

For some traces in 2011, river water samples intended for SF_6 analysis in the U.K. were also collected in 120 ml Wheaton vials filled with 120 ml water and sealed with rubber stoppers

(following Busenberg and Plummer[7]). In the laboratory, a 20 ml headspace was created by inserting two needles through the stopper: one long needle inserted to the base of the vial and a short needle which only just protruded. 20 ml of 100% N_2 gas at room temperature and pressure was injected from a gas-tight syringe into the Wheaton vial through the short needle, and displaced water was pushed out through the long needle. Both needles were then removed. Vials were shaken for 10 minutes on an automatic shaker and then left overnight in an incubator at 15°C to equilibrate.

All samples were analysed using a portable Cambridge Scientific 200-Series Gas Chromatograph (GC) fitted with an electron capture detector (ECD). The GC was calibrated on the day of analysis using a 1.09 or 1.30 ppb SF_6 standard (except 15, 17 and 21 June 2010, when 5.0 ppb was used), assuming a linear calibration.

ECD linearity is subject to some uncertainty in previous work employing SF_6 tracing, with the range of the linear region varying widely between studies[8-10] or not reported[11,12]. For example, Dillon and others[9] found the linear range extended over four orders of magnitude (0.04 to 42.53 pmol of SF_6 injected into the column), while at the other extreme Vulava and others[10] used several standards to establish a quadratic calibration curve from 10^{-9} to 10^{-5} g SF_6 (or 7 to 70,000 pmol). In practice, our peak SF_6 concentrations were within a factor of 10 of the standard for 26 out of 28 traces, with the remaining 2 having lower peak concentrations (0.04 and 0.05 ppb on 19 July and 12 August 2009, respectively) probably due to short hose lengths (50 m) being used during testing at L1 in 2009. Diluting the 1.09 ppb standard by a factor of ~10 with pure N_2 showed the ECD response (expressed as peak area in the chromatogram) remained linear at these lower concentrations (Fig. S1.2).

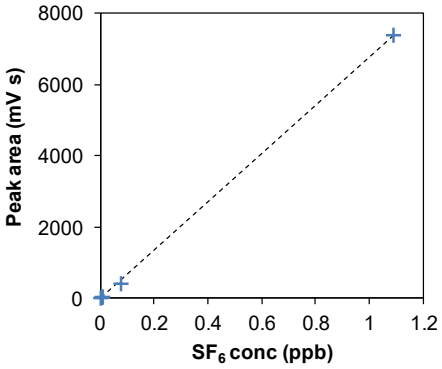

Fig. S1.2: *Diluting the 1.09 ppb standard by a factor of 10 shows the ECD detector response (blue crosses) is close to the linear approximation (dashed line).*

Repeat measurements and analysis of the diluted standard yielded an analytical precision (1σ) of 2% and a limit of detection of 0.015 pptm in water, respectively. All traces used in this paper displayed peak SF_6 concentrations at least an order of magnitude above background levels. Sample SF_6 concentrations were calculated as follows, for both methods (Wheaton vial or syringe). First, the headspace SF_6 concentration $c_{SF6(h)}$ (in pptv), when assuming a linear detector response, is

$$c_{SF6(h)} = c_{std} A_{smp} / A_{std}, \qquad [S1.1]$$

where A_{std} and A_{smp} are the peak areas measured by the GC for the standard (c_{std} = 1090 pptv SF_6) and sample, respectively. Assuming SF_6 behaves as an ideal gas, the number of moles of SF_6 in the headspace is

$$n_{SF6} = c_{SF6(h)} \times PV_h/\mathrm{RT}. \qquad [S1.2]$$

Here, T and P are the headspace temperature and pressure at time of creation, V_w is the headspace volume and R = 8.314 J mol^{-1} K^{-1} is the ideal gas constant. If the SF_6 is partitioned between the water and headspace such that a fraction k is in the headspace at equilibrium, then the original SF_6 concentration in the water (in pptm or ng/kg) is

$$c_{SF6(w)} = n_{SF6} \times m/(kV_w\rho_w) \qquad [S1.3]$$

where V_w is the volume of sample water remaining after the headspace volume V_h is added, the density of water is ρ_w = 1000 kg m^{-3}, and the molar mass of SF_6 is m = 146.06 g mol^{-1}.

S2. TRACER DATA PROCESSING

S2.1 Dye traces

The measured fluorescence signal was a combination of the dye signal and natural fluorescence of suspended sediments (Fig S2.2). This natural background varied slowly with time and needed separating from the dye return. First, the approximate period of the tracer return was identified by visual inspection. Next, two series of concentrations (usually with a minimum of 5 points each) were selected from before and after the passage of the peak. For the majority of dye returns with only slow changes in background fluorescence, a linear least-squares regression equation was calculated for these selected points, and was used to estimate the change in background signal during the course of the tracer return. This background was then removed from the observed values. If the measured, background and background-corrected fluorometer voltages are $V_m(t)$, $V_b(t)$ and $V_c(t)$, then

$$V_b(t) = at + b$$
$$V_c(t) = V_m(t) - V_b(t) \qquad [S2.1]$$

where a and b are the linear regression parameters. The corrected voltages $V_c(t)$ were converted to dye concentration using the empirical calibration described above (Section S1).

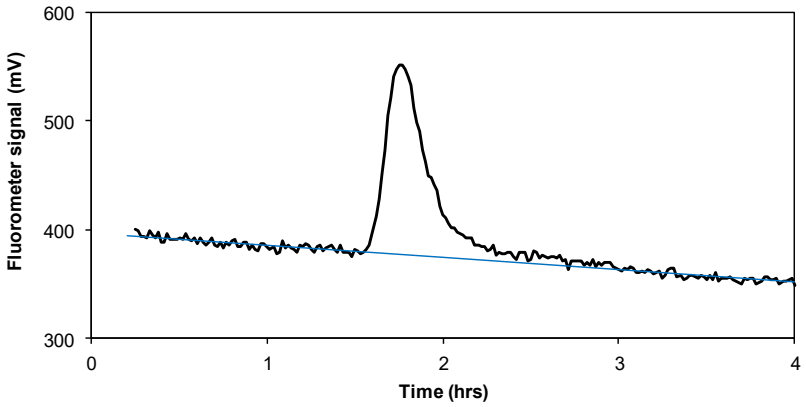

Fig. S2.1: *Example dye trace from L7, 21 June 2010, showing the measured fluorometer signal V_m (black line) and inferred background V_b (blue line).*

In some cases the fluorometer readings were subject to a highly variable background, which could not be removed using the above method. In these cases it was also difficult to identify the start and end of the peak, leading to considerable uncertainty in some (but not all) parameter values extracted from the trace (see Section S2.3 below).

S2.2 SF_6 traces

The long tails of the SF_6 breakthrough curve commonly prevented clear identification of the return to background concentrations, so instead the measured SF_6 concentrations were background corrected by subtracting a constant value c_b defined as the mean concentration of samples collected prior to the arrival time t_a of the tracer return, i.e.,

$$c_b = \overline{c_m(t)}; t < t_a$$
$$c_c(t) = c_m(t) - c_b;\ t > t_a \qquad [S2.2]$$

S2.3 Tracer velocity and dispersivity

In most previous tracing studies in glaciology (e.g. Seaberg and others[3]), the mean tracer velocity and dispersivity have been calculated by assuming a 1-dimensional advection-dispersion model for tracer transport through the drainage system. With constant water velocity and dispersion along the flow path, and zero storage, reaction or tracer loss, the concentration c of a tracer is described by the 1-dimensional advection-dispersion equation:

$$\frac{\partial c}{\partial t} = D\frac{\partial^2 c}{\partial x^2} - v\frac{\partial c}{\partial x} \qquad [S2.3]$$

where x is the distance along the flow path, v is the mean water velocity and D is the coefficient of longitudinal dispersion. Further assuming that the initial tracer concentration at the time of injection

($t = 0$) can be represented by a delta function, which is a good approximation for slug injections, the tracer concentration c expressed in kg m^{-3} is given by:

$$c(x,t) = \frac{mv}{Q(4\pi Dt)^{1/2}} \exp\left[-\frac{(x-vt)^2}{4Dt}\right] \qquad \text{[S2.4]}$$

where Q is the discharge, m is the mass of tracer injected and v is the water velocity. In the case that storage cannot be neglected (for example if there is tracer storage in eddies, low-velocity regions next to conduits, or tracer adsorption onto sediments[3]), the breakthrough curve will have a long, drawn-out tail once the main peak has passed. To minimise the effects of these processes on calculations, the key hydraulic properties (dispersion coefficient, dispersivity, water velocity) have often been calculated from tracer returns following the method of Seaberg and others[3], who used only the main peak rather than the full return. This is achieved by identifying two times (t_1 and t_2) when the tracer concentration is at half its peak concentration, from which the dispersion coefficient is calculated using:

$$D = \frac{x^2(t_m - t_j)^2}{4t_m^2 t_j \ln \tau_j} \qquad \text{[S2.5]}$$

where t_m is the time of peak concentration, $\tau_j = 2(t_m/t_j)^{1/2}$, $j = 1$ denotes the rising limb and $j = 2$ denotes the falling limb. Although t_m can be estimated from the tracer return, it is treated as an unknown, giving two equations for two unknowns. Seaberg and others[3] found the solution iteratively by trial and error. Alternatively we can combine the two equations for D at times t_1 and t_2 to yield an equation in t_m:

$$f(t_m) = \frac{x^2(t_m - t_1)^2}{4t_m^2 t_1 \ln \tau_1} - \frac{x^2(t_m - t_2)^2}{4t_m^2 t_2 \ln \tau_2} = 0 \qquad \text{[S2.6]}$$

Eq. S2.6 can be conveniently solved using the Newton-Raphson method, i.e.,

$$f\left(t_{m(k+1)}\right) = t_{m(k)} - \frac{f\left(t_{m(k)}\right)}{f'\left(t_{m(k)}\right)} \qquad [S2.7]$$

where k is the iteration number and the derivative $f'(t_m) = \mathrm{d}f(t_m)/\mathrm{d}t_m$ is:

$$f'\left(t_m\right) = \frac{2\left(t_m - t_1\right)\ln\tau_1 - \left[\frac{\left(t_m - t_1\right)^2}{2t_m}\right]}{t_1\left(\ln\tau_1\right)^2} - \frac{2\left(t_m - t_2\right)\ln\tau_2 - \left[\frac{\left(t_m - t_2\right)^2}{2t_m}\right]}{t_2\left(\ln\tau_2\right)^2} \qquad [S2.8]$$

Times t_1 and t_2 were obtained by linear interpolation of the tracer return curve. In the rare event that there was more than one value of t_1 or t_2 then the mean of all possible values was used. With a starting value of $t_{m(0)} = ½(t_1+t_2)$, Eq. S2.7 generally converged to a solution (defined as being when $|t_{m(k+1)} - t_{m(k)}|$ was less than the machine precision) within 4 iterations. Finally, the 'average' water velocity $v = x/t_m$.

The above method for determining v and D is suitable for data where (1) the signal-to-noise ratio is low; (2) the data are collected at high temporal resolution; and (3) the 1-D advection-dispersion model is appropriate. Many previous dye tracing studies in glaciers, as well as some of those in the present study, have satisfied these requirements. However, for many traces in this study the velocity and dispersivity are unlikely to be constant along the flow path, and SF_6 is subject to the problem of degassing (see Section S2.4 below). Furthermore, in practice the values of both v and D depend largely on a maximum of 5 individual data points: these are the 2 points either side of the time at which c passes $c_{max}/2$ during the rising limb, the equivalent 2 points on the falling limb, and the value of c_{max}. Clearly, for discrete data with low temporal resolution such as those generated by SF_6 sampling, or for data with considerable noise, or for systems with un-steady or spatially-variable flow properties, this method may suffer from large errors.

A better approach is to identify times at which a given percentage of the returned tracer has passed, since this time will depend upon all of the data points and requires no assumption on the form of the

breakthrough curve. For example, we can define v_{05} and v_{50} as the velocities corresponding to the times t_{05} and t_{50} at which 5% and 50% of the returned tracer has passed, respectively; here these values are interpreted as the maximum and mean velocities. The latter is widely employed in tracing studies and is often called the 'centroid' velocity. Both v_{05} and v_{50} can be conveniently obtained from interpolation of the cumulative tracer return, and are free from the restrictive assumptions implicit in the t_1, t_2 method. Following the same arguments, instead of measuring the tracer dispersion by the parameter D, we can alternatively measure dispersion using v_{05} and v_{50} by calculating the normalised velocity difference $\Delta v = (v_{05} - v_{50})/ v_{50}$. Similarly to D, Δv is zero in the case of advection with zero dispersion, increases as the peak gets broader and tends to infinity in the limit of high dispersion with negligible advection.

The arrival times described in the paragraph above are illustrated in Fig. S2.2.

In the case of incomplete traces where the full tail was not captured, the cumulative return could not be calculated and instead v_{05} was estimated from the arrival time of the tracer. By testing this approximation on complete traces, we found the error associated with this approach to be less than 10%.

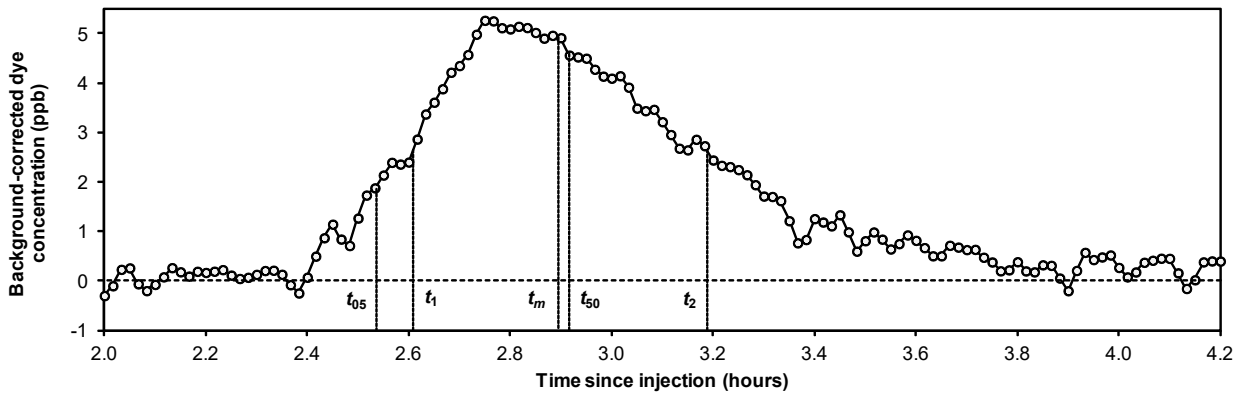

Fig. S2.2: *Example dye trace from L7 (15 June, 2010) showing the various times used when calculating the return curve parameters defined in Section S2.*

Dye traces from L7 and L14 emerged over several hours, during which time the background fluorescence of the river during some traces varied over a range of similar order of magnitude to the dye fluorescence. Extracting the dye signal was therefore problematic, since subtracting a linear background was not appropriate. Experimenting with different peak start and end times, and with several background correction curves modelled by fitting polynomials to the inferred background, showed that the maximum and mean velocities were relatively insensitive to choice of background (for example 0.96 to 0.98 m s^{-1} and 0.79 to 0.82 m s^{-1}, respectively, on 7 June 2010), but that values of D were more uncertain (98 to 133 m s^{-2}) (Fig S2.3). Therefore, the tracer velocity estimates were retained for subsequent analysis, but not the dispersivity. Traces where dye concentrations calculated in this manner were as follows: L7, 9 August 2009; L7, 31 May 2010; L14, 3 June 2010; L14, 7 June 2010.

Tracing data collected in all three years are summarised fully in Tables S1a, S1b and S1c and presented in Figs S2.4 to S2.8.

S2.4 SF_6 retardation

In the tracer results (Figs. S2.4 to S2.6), there was often a noticeable lag in the SF_6 peak relative to the dye peak for dual traces (i.e., traces when both dye and SF_6 were injected simultaneously). This retardation highlights one of the important differences between the two tracers, namely the volatility of SF_6, which promotes its degassing into any headspace existing between the water in the channel and the overlying ice roof. One of the crucial assumptions of using tracers to measure flow characteristics is that the tracer travels with the water, therefore retardation limits some (but not all) information that can be acquired about the drainage system when using SF_6 independently. For this reason, we do not pursue a number of calculations from SF_6 breakthrough curves that would normally be employed (e.g. for dispersivity). However, our work clearly shows that the first arrival time for SF_6 is not affected by retardation: in dual traces from L7 and L14, the maximum tracer

velocity was almost identical for both tracers, even though subsequent tracer emergence and average velocities were very different in some cases (see Fig S2.7). Specifically, the root mean-square (RMS) error between the n paired dye and SF_6 v_{05} values, i.e. $[\Sigma(v_{05,dye} - v_{05,SF6})^2/n]^{1/2}$, is 0.055 m s^{-1}, which is a factor of 5 smaller than standard deviation of dye v_{05} values (0.27 m s^{-1}). Therefore, we conclude that using v_{05} measure of tracer velocity is not subject to the problems of degassing and retardation, which is the reason for us having chosen the 'maximum' velocity as the measure of water flow properties in the main text, rather than the more conventional 'average' velocity. We have not discussed in detail properties such as dispersivity for the SF_6 traces, which in the past have been employed as useful measures of water flow properties for shorter experiments with non-volatile tracers.

The limitations imposed by SF_6 retardation can also become advantages in dual traces. Retardation due to tracer volatility in small-scale column experiments has been shown to depend largely on the water saturation in porous materials[10]; extrapolating these results to the scale of the subglacial drainage system suggests retardation would be expected to increase at lower water pressures, when air spaces are more likely. Under this assumption we can use retardation as an indicator of channel pressurisation between the moulin and portal. Here, retardation is quantified as the ratio of average velocities, i.e., $R_{50} = v_{50,dye} / v_{50,SF6}$. Results summarised in Table S1 and plotted in Fig. 2 show R_{50} is greatest near the margin (Moulin L1) and decreases rapidly inland, becoming very small by Moulin L14 even though water from these longer traces travels through the same marginal portion of the drainage system. At present we have two possible explanations for this result. First, the water draining into moulins near the margin still has to travel through small englacial and probably subglacial channels before connecting with the main channel. It could be these initial reaches that contribute most to the retardation if the water table is very low near the margin. In this case the retardation occurs prior to the tracer reaching the main channel(s), and its effects are preserved in the breakthrough curve owing to the very limited dispersion in the short time spent by the tracer in the main channel. Second, if the 'open channel' flow is restricted to the final few hundred metres

(residence time likely to be <10 minutes at typical flow rates), this section would have a much greater *relative* effect on traces of 1 km emerging over tens of minutes than those of 40 km emerging over tens of hours.

Although we are unsure as to which of these explanations best describes our results, we note that both require the water pressure to be relatively low close to the margin. Since this is a physically reasonable and unsurprising result, it provides extra confidence that the SF_6 tracing can provide an accurate picture of drainage system characteristics.

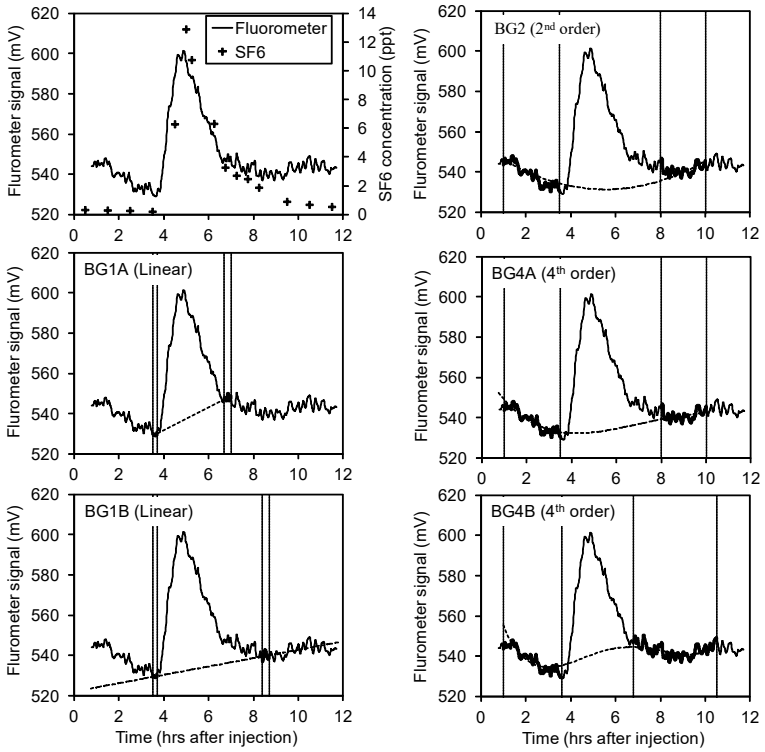

Figure S2.3. *Top left: raw fluorometer output and SF_6 concentrations for the L14 trace on 7 June 2010. Owing to the noisy fluorometer background, subtracting a linearly varying background (BG1A; BG1B) before calculating dye concentrations is clearly inappropriate. Instead, it is possible to fit various higher-order polynomials (for example BG2; BG4A; BG4B) to the background. Background concentrations were specified between the two pairs of vertical lines, and the inferred background is shown by the dashed line. Since there is uncertainty regarding the behaviour of the background and also the timing of the end of the peak, corresponding values of D in each case vary widely (98 to 133 $m^2\ s^{-1}$); however, calculated velocities are much less variable (v_{05}: 0.96 to 0.98 $m\ s^{-1}$; v_{50}: 0.79 to 0.82 $m\ s^{-1}$). Consequently, dispersion values measured by ΔV (0.18 to 0.23) vary less widely than those of D.*

Site	Date	Time	Mass SF_6/dye (kg)	Q ($m^3\ s^{-1}$)	σ_Q ($m^3\ s^{-1}$)	ΣQ (m^3)	v_{05} SF_6/dye ($m\ s^{-1}$)	v_{50} SF_6/dye ($m\ s^{-1}$)	D dye ($m^2\ s^{-1}$)	ΔV SF_6/dye	R_{50}
L1	19 Jul[1]	1730	0.34 / 0.60	273	3.0	4.3×10^8	1.06 / 1.51	0.36 / 1.33	2.5	1.98 / 0.14	3.72
	4 Aug[2]	1350	0.34 / 0.80	175	4.0	7.2×10^8	0.90 / 1.76	0.35 / 1.29	11.2	1.59 / 0.36	3.71
	6 Aug	1340	0.34 / 0.80	182	3.8	7.5×10^8	1.29 / 1.87	0.37 / 1.42	16.2	2.52 / 0.32	3.88
	7 Aug	1010	0.34 / 0.80	175	2.3	7.6×10^8	0.68 / 1.09	0.23 / 0.94	7.6	1.90 / 0.16	4.02
	8 Aug	1825	0.34 / 0.80	202	2.1	7.8×10^8	1.26 / 1.67	0.44 / 1.37	16.0	1.85 / 0.22	3.09
	12 Aug[1]	1130	0.34 / 0.80	189	4.9	8.4×10^8	0.90 / 1.80	0.33 / 1.55	12.5	1.69 / 0.16	4.64
	13 Aug	1122	0.34 / 0.80	195	4.7	8.6×10^8	0.92 / 0.92	0.31 / 0.85	2.2	1.96 / 0.08	2.74
L7	9 Aug[3]	1545	2.0 / 3.0	201	4.8	8.0×10^8	0.91 / 0.95	0.53 / 0.82	—	0.78 / 0.16	1.56
	17 Aug	1315	2.0 / 8.0	183	5.1	9.3×10^8	0.89 / 0.90	0.55 / 0.84	6.6	0.60 / 0.07	1.51

Table S1a. Summary of tracing data collected in 2009. Times are local (UTC – 2 hrs). Mass is the mass of tracer injected; Q and σ_Q are the mean and standard deviation of the Leverett river discharge during the trace; ΣQ is the season's cumulative discharge; v_{05} and v_{50} are the maximum and mean tracer velocities (see Section S2.3 for definitions); D and ΔV are measures of tracer dispersivity (also defined in Section S2.3); R is the retardation of SF_6 expressed as a ratio of the respective v_{50} values for dye and SF_6.

(1) Hose length 50 m (length in most traces was 150 m)

(2) Hose length 100 m

(3) Variable background in dye return; calculation of D not possible.

Site	Date	Time	Mass SF_6/dye (kg)	Q ($m^3\ s^{-1}$)	σ_Q ($m^3\ s^{-1}$)	ΣQ (m^3)	v_{05} SF_6/dye ($m\ s^{-1}$)	v_{50} SF_6/dye ($m\ s^{-1}$)	D dye ($m^2\ s^{-1}$)	ΔV SF_6/dye	R_{50}
L1	31 Jul	1100	0.20 / 0.60	376	5.9	1.4×10^9	0.66 / 0.66	0.47 / 0.61	1.10	0.39 / 0.07	1.30
	11 Aug	1110	0.20 / 0.60	284	3.7	1.6×10^9	0.53 / 0.56	0.40 / 0.53	0.69	0.32 / 0.07	1.33
	11 Aug	1830	0.20 / 0.60	275	1.6	1.6×10^9	0.34 / 0.44	0.26 / 0.42	1.13	0.27 / 0.06	1.62
	15 Aug	1100	0.20 / 0.60	237	5.2	1.7×10^9	0.43 / 0.51	0.32 / 0.47	0.91	0.35 / 0.07	1.47
L7	31 May[1]	1740	— / 5.0	87	0.9	7.0×10^7	— / 0.74	— / 0.53	—	— / 0.35	—
	9 Jun	1412	1.0 / 4.0	203	2.7	1.7×10^8	1.03 / 0.99	0.78 / 0.83	27.4	0.33 / 0.20	1.07
	15 Jun	1325	1.0 / 4.0	187	1.2	2.8×10^8	0.87 / 0.83	0.69 / 0.72	20.1	0.26 / 0.15	1.04
	21 Jun	1400	1.0 / 3.6	185	2.1	3.8×10^8	1.29 / 1.28	1.08 / 1.16	14.5	0.19 / 0.10	1.08
	4 Jul	1529	— / 3.0	304	3.8	6.7×10^8	— / 1.58	— / 1.47	12.7	— / 0.08	—
	16 Jul	1451	— / 3.0	282	3.1	9.7×10^8	— / 1.26	— / 1.17	9.16	— / 0.08	—
	30 Jul	1425	— / 2.0	390	4.1	1.3×10^9	— / 1.45	— / 1.33	14.5	— / 0.09	—
	12 Aug	1200	— / 2.0	275	5.6	2.1×10^9	— / 1.99	— / 1.83	21.7	— / 0.09	—
L14	3 Jun[1]	1300	4.0 / 12.0	109	5.0	9.4×10^7	0.43 / 0.44	0.36 / 0.39	—	0.18 / 0.11	1.08
	7 Jun	1630	4.0 / 12.0	134	6.4	1.4×10^8	1.08 / 0.96	0.72 / 0.81	98.1	0.49 / 0.18	1.12
	19 Aug	1100	— / 12.0	244	4.7	1.8×10^9	— / 1.42	— / 1.32	24.6	— / 0.08	—
IS35	17 Jun[2]	1130	4.0 / —	—	—	—	0.44 / —	— / —	—	— / —	—

Table S1b. Summary of tracing data collected in 2010. For description of column headings see Table S1a.
(1) Variable background in dye return so calculation of D not possible (see Section S2.4).
(2) Trace to Issunguata Sermia. No discharge measurements available for this catchment. Only the onset of the trace was sampled, so v_{05} estimated from the first arrival time.

Site	Date	Time	Mass SF_6 (kg)	Q ($m^3\ s^{-1}$)	σ_Q ($m^3\ s^{-1}$)	ΣQ (m^3)	v_{05} SF_6 ($m\ s^{-1}$)	v_{50} SF_6 ($m\ s^{-1}$)	ΔV SF_6
L7	13 Jun[1]	1830	0.1	49	2.4	1.9×10^7	0.39	0.31	0.26
	15 Jun[1]	1200	0.1	74	2.7	2.7×10^7	0.39	0.31	0.26
	17 Jun[1]	1215	0.1	131	4.2	4.5×10^7	0.47	0.38	0.25
	19 Jun[2]	1545	1.1	148	3.0	7.0×10^7	0.67	0.50	0.33
L41[4]	26 Jun[3]	1440	5.7	165	11.7	1.7×10^8	0.25	—	—
	1 Jul	1505	3.6	169	10.4	2.5×10^8	0.35	0.27	0.33
	4 Jul	1525	3.9	162	9.6	2.9×10^8	0.38	0.30	0.26
	1 Aug[3]	0915	2.9	227	10.0	7.8×10^8	1.04	0.78	0.33
L57	12 Aug[3]	2035	9.0	224	6.3	1.0×10^9	0.22	—	—

Table S1c. Summary of tracing data collected in 2011. For description of column headings see Table S1a.
(1) Trace injected using the saturated tank method (see Section S2.1).
(2) Hose length 50 m.
(3) Incomplete trace: v_{05} estimated from first arrival.
(4) Hose length 100 m.

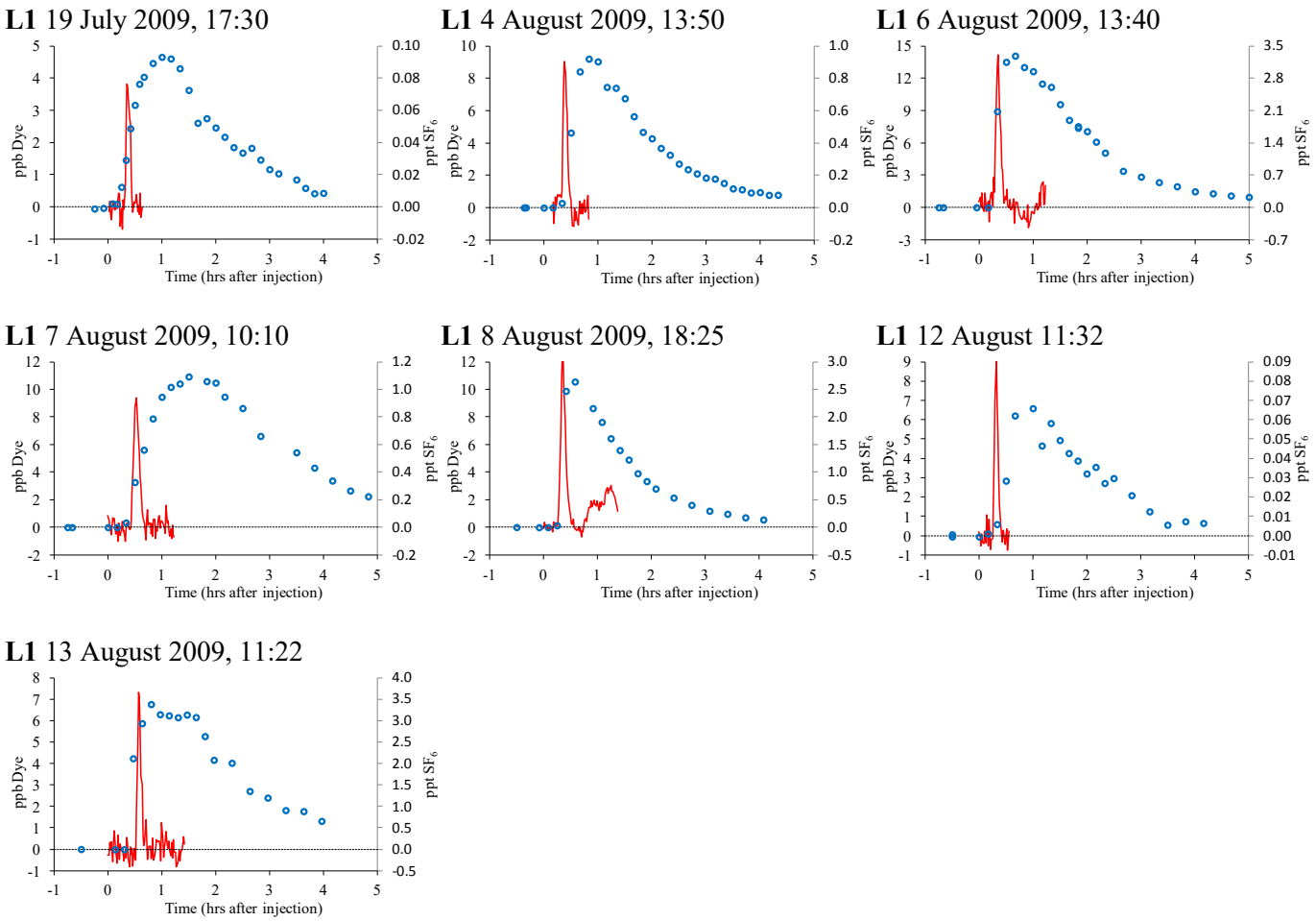

Figure S2.4a. *Dye (red lines) and SF_6 (blue circles) traces from L1 in 2009. Dye concentrations were recorded at 1 minute intervals; SF_6 concentrations were measured in discrete samples represented by individual data points.*

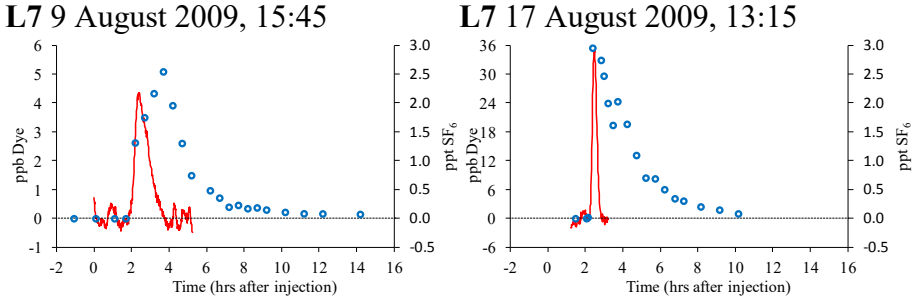

Figure S2.4b. *Traces from L7 in 2009. Symbols follow Fig. S2.4a.*

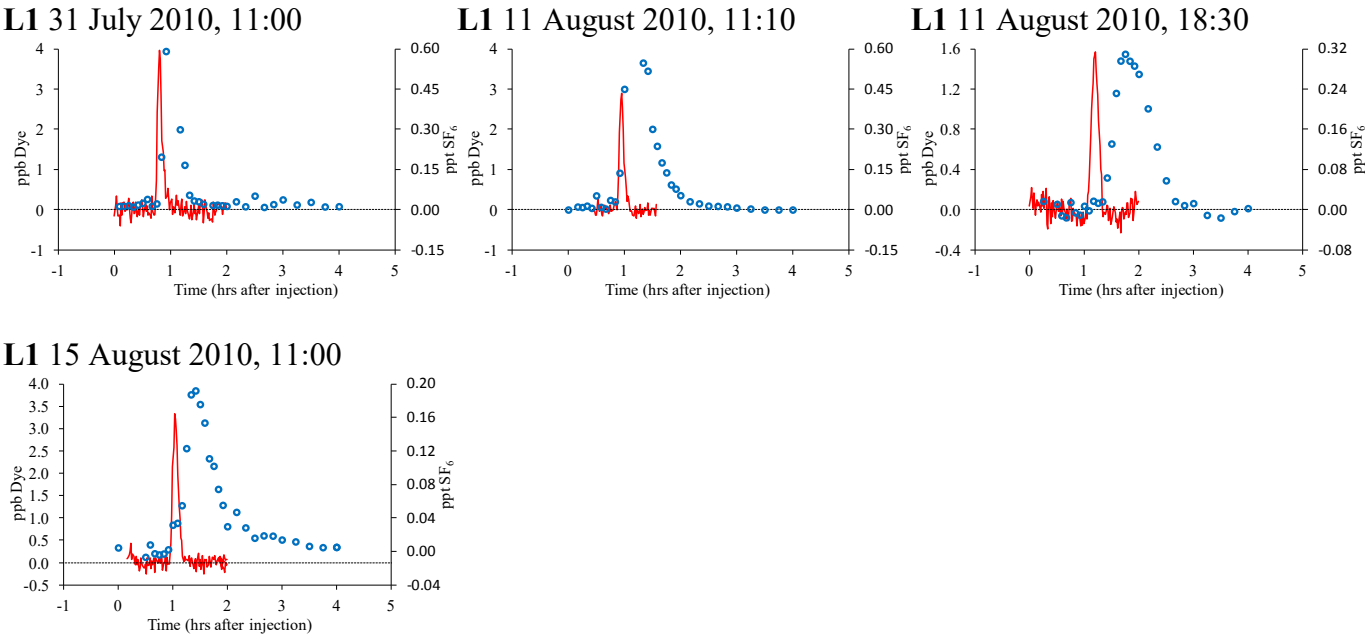

Figure S2.4c. *Traces from L1 in 2010. Symbols follow Fig. S2.4a.*

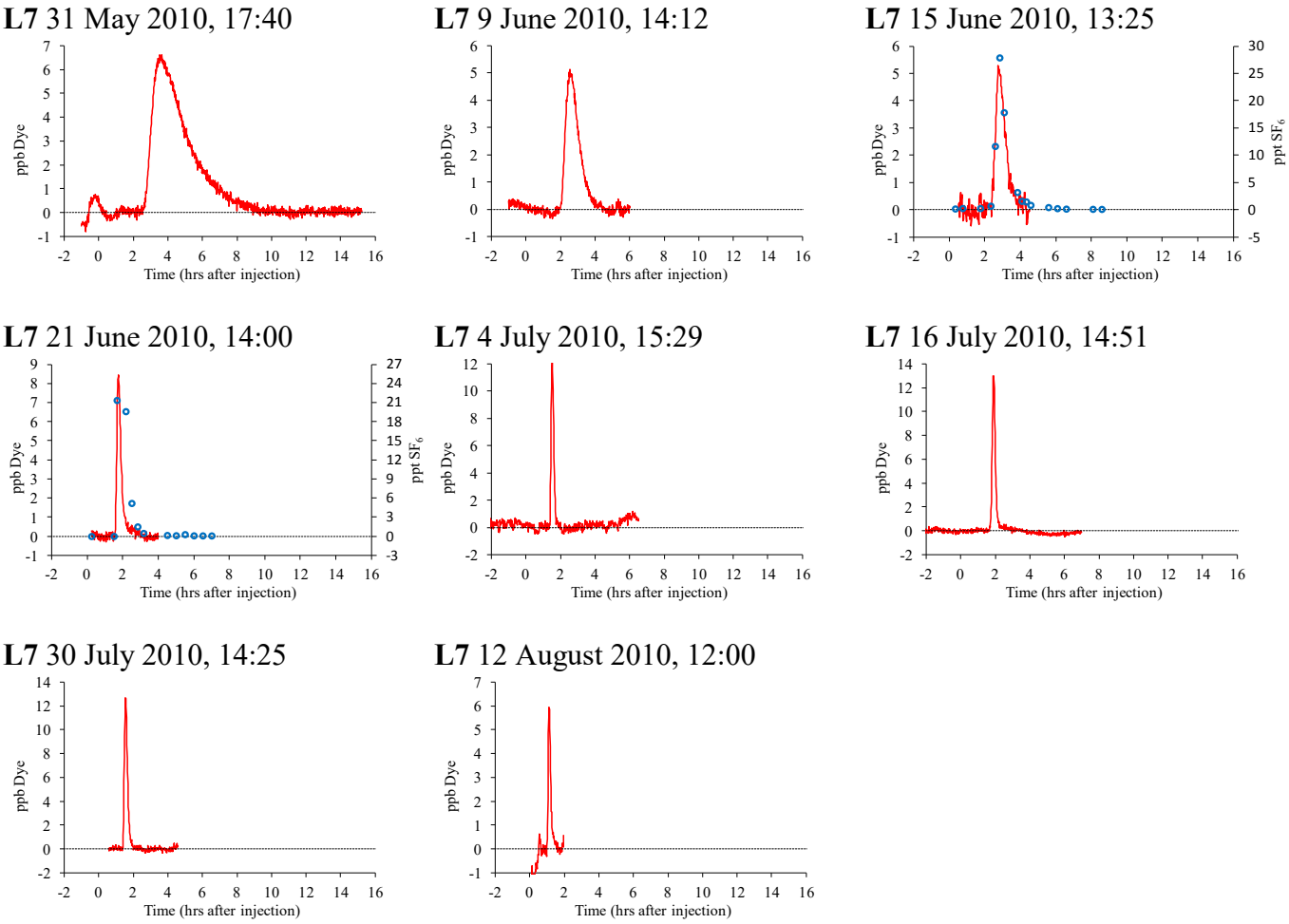

Figure S2.4d. *Traces from L7 in 2010. Symbols follow Fig. S2.4a.*

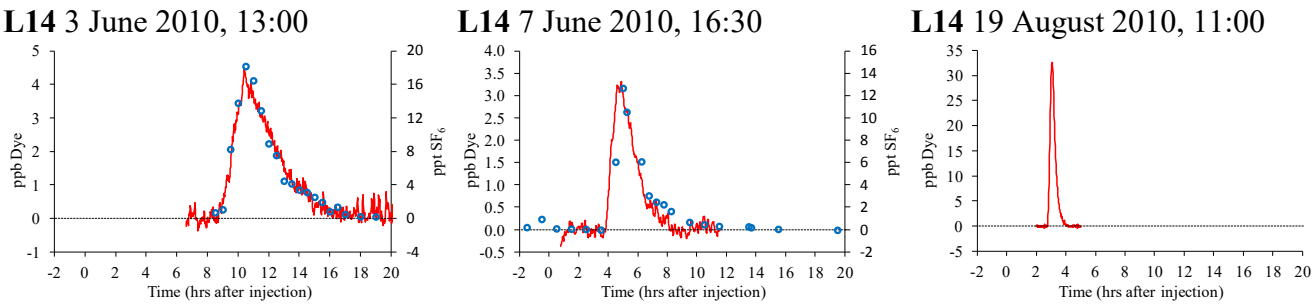

Figure S2.4e. *Traces from L15 in 2010. Symbols follow Fig. S2.4a.*

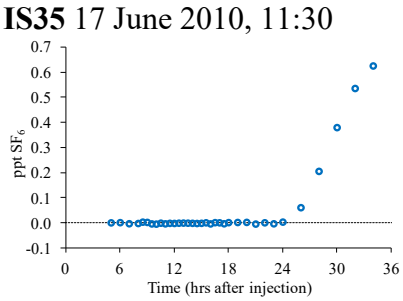

Figure S2.4f. *Trace from IS39 in 2010. Symbols follow Fig. S2.4a. Samples were collected at the terminus of Issunguata Sermia for later analysis at Leverett Glacier; the trace emerged later than expected and is therefore incomplete.*

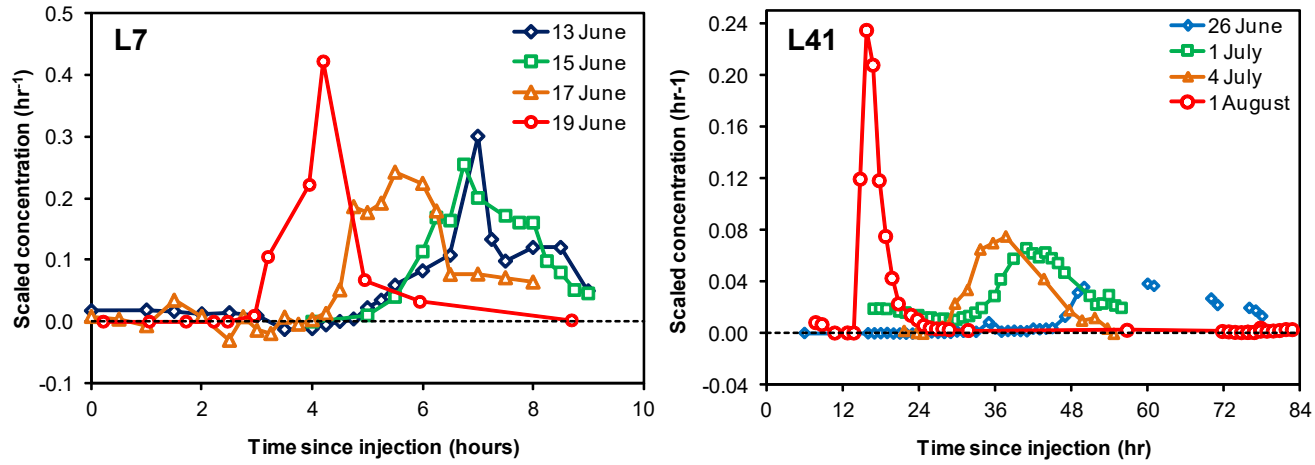

Figure S2.5. *SF_6 traces from L7 and L41 in 2011. Tracer returns have been scaled to have unit area.*

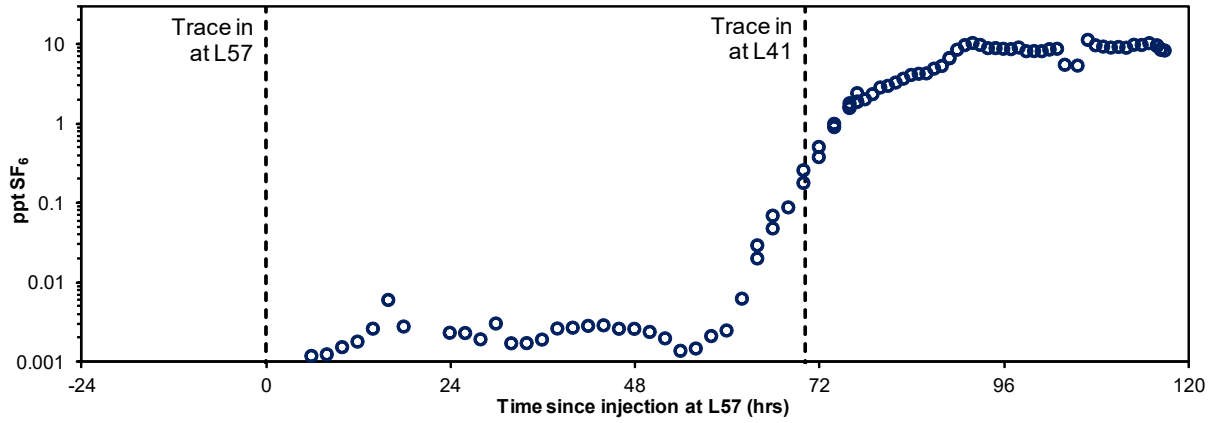

Figure S2.6: *SF_6 returns from the last two traces in 2011, at L57 (12 August, 20:30) and L41 (15 August, 18:30). Water samples for both traces were collected in bottles for analysis in the U.K., and the later than expected arrival of the L57 trace unfortunately interfered with the subsequent L41 trace. However, the arrival of the L57 trace prior to injection of the L41 trace enables an estimate of the maximum velocity of the L57 trace (0.22 m s^{-1}). Given the rapid passage of previous L41 traces in < 24 hr (see Fig. S2.4) it is likely that most of the sustained, high SF_6 concentrations are due to the L57 trace; however, this cannot be confirmed. Noting the log scale, we find that the SF_6 analysis method employed in this study can yield data with apparently low noise levels over 4 orders of magnitude.*

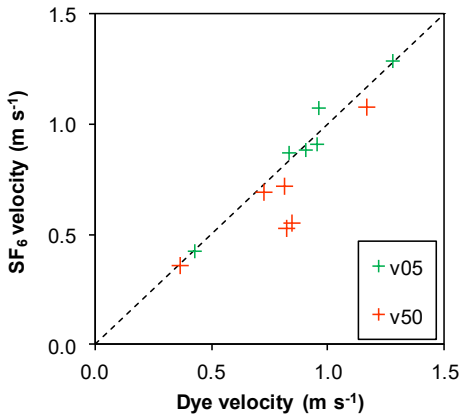

Figure S2.7*. Comparison of tracer velocities in dual traces from moulins L7 and L14. v_{05} and v_{50} represent the maximum and mean tracer velocities, respectively. Traces close to the dashed line yielded similar velocities for dye and SF_6.*

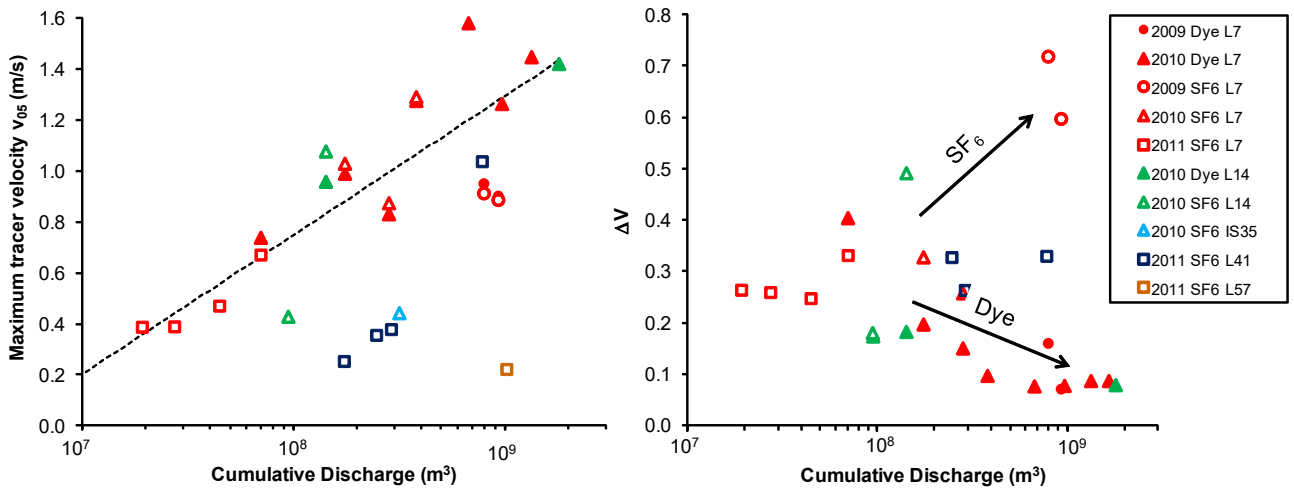

Figure S2.8: *Evolution of tracer velocity and dispersion with time. While maximum velocities for SF_6 are shown to be representative of the water flow (see text), the dispersion values can be strongly influenced by degassing and are not reliable estimates of the true values: instead they may reflect drainage system pressurisation. Time is measured by cumulative discharge to allow comparison between years with different timing and intensity of surface melt. The dashed line in the left panel is the regression curve for Site L7, which has the form $v_{05} = A\ln(\Sigma Q) + B$ where v_{05} is the maximum velocity (here corresponding to the time at which 5% of the recovered tracer had emerged) and A, B are regression parameters ($A = 0.235$ m s^{-1}, $B = -3.59$ m s^{-1}; $r^2 = 0.63$, $p < 0.01$). See Section S2 for definitions of velocity and dispersion.*

S3. RIVER AND MOULIN FLOW RATES

S3.1 River flow rate

Discharge of the river emerging from the terminus of Leverett Glacier was monitored each summer using a pressure transducer (to continuously record water depth, at 10 minute intervals) and regular dye dilutions (to establish a rating curve between water depth and discharge). Full details of the river gauging at Leverett have been described previously[13]. Discharge and cumulative discharge are shown in Fig. S3.1. Because the onset of melt varied widely between the three years, the cumulative discharge was used as a measure of time when exploring the seasonal evolution of tracer velocities.

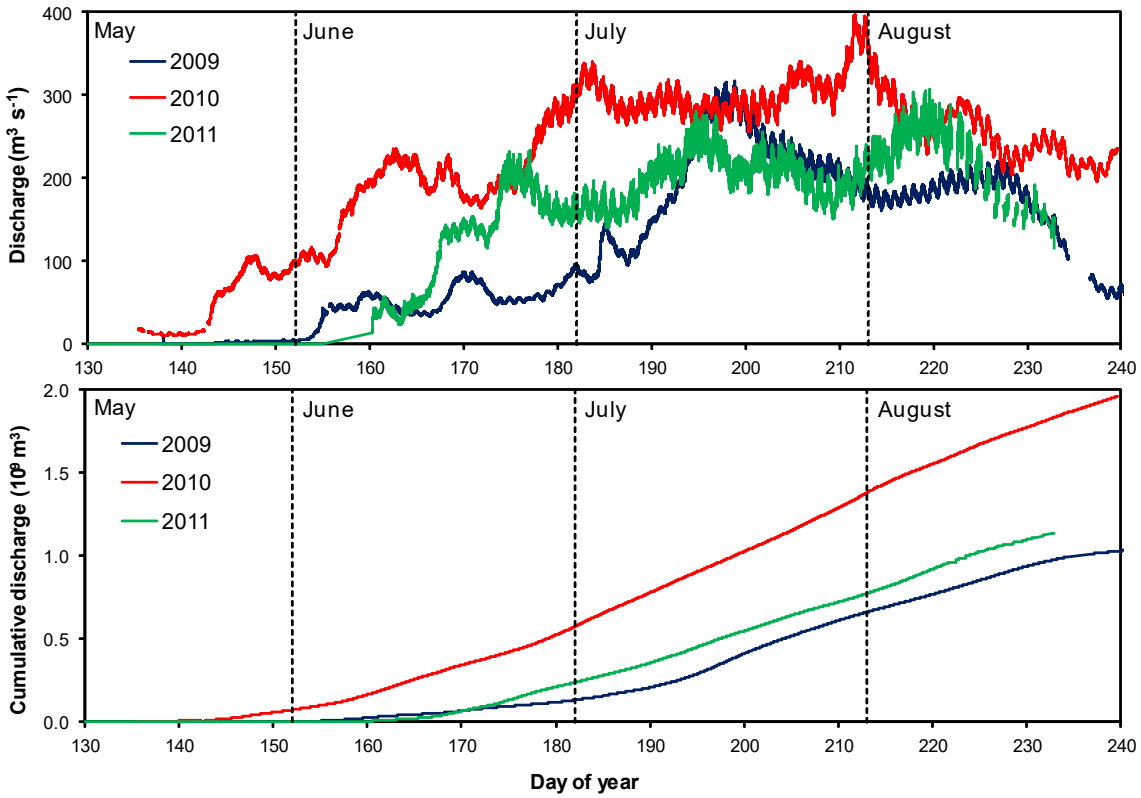

Figure S3.1: *Discharge and cumulative discharge of the river emerging from Leverett Glacier, 2009 to 2011.*

S3.2 Moulin flow rate (summer 2011 only)

Moulin flow rates were recorded at L41 and L57 using the same stream gauging approach as that used for river flow rate, except that here salt (sodium chloride) and an electrical conductivity (EC) sensor were used in place of rhodamine dye and the fluorometer. Salt is an excellent tracer for supraglacial streams because the natural EC is very low (order 2 μS cm^{-1} in 2011). To measure flow rate, a known amount of salt (50 – 200 g) was dissolved in a bucket and injected into the stream 100 – 200 m upstream of an EC sensor installed close to the moulin. A pressure transducer was installed next to the EC sensor, to record water depth. Pressure and EC were logged on a Campbell Scientific CR10X data logger at 1 minute intervals (increasing to 5 s intervals during injections).

During the first observation period at L41 (Days 180 – 188 or 29 June – 7 July) a total of 14 salt dilutions yielded a power law fit between pressure transducer output and discharge of the form Q =

aP^b (a = 2.46 mV^{-b}, b = 1.58; r^2 = 0.96; p < 0.01: Fig. S3.2a). The residuals to this regression line were not correlated with time, so we have not corrected for the effects of melt on channel geometry. These effects were presumably small during this period, given the high r^2 value. During the shorter second period (Days 229 – 231 or 17 – 20 August), the pressure probe was installed in the same stream but in a slightly wider section with lower turbulence (hence the less noisy record). Since only 4 dilutions are available for this time interval, we assumed the same power law function and exponent b, and used least squares only to determine the co-efficient a. This yielded a = 22.6, b = 1.58; r^2 = 0.97; p < 0.01 (Fig. S3.2b). Given the distribution of points in Fig. S3.2b, we question the validity of the r^2 value in this case, acknowledging that there is clearly greater uncertainty associated with mid-range flow rates for this period than for the earlier period.

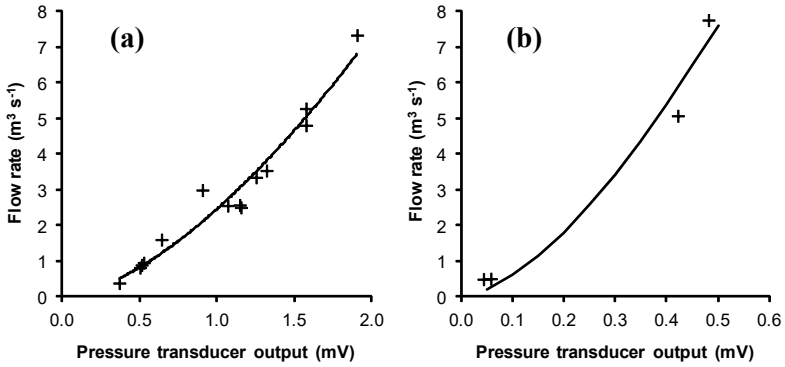

Figure S3.2: *Rating curves to convert pressure transducer output to flow rate at Moulin L41, based on salt dilution gauging, for 29 June – 7 July (a) and 17 – 20 August (b).*

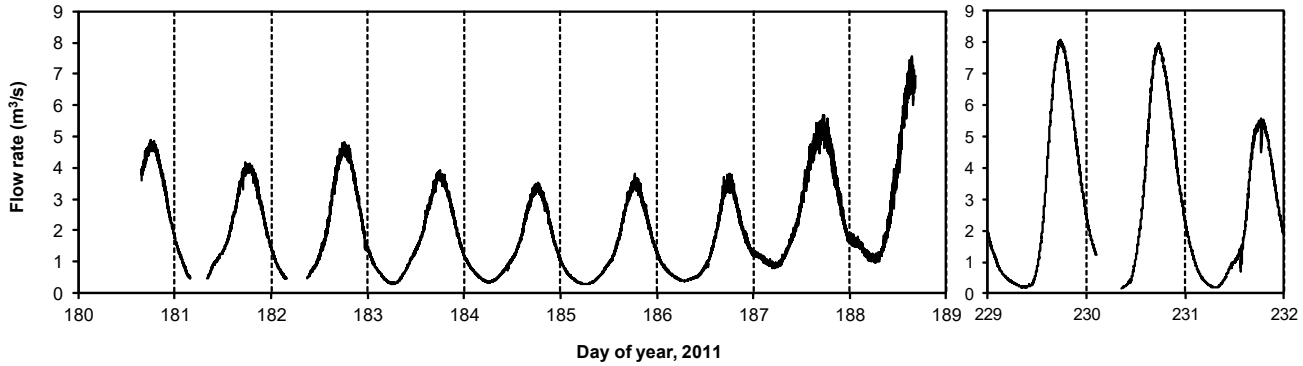

Figure S3.3: *Flow rate into Moulin L41, calculated by converting pressure probe readings to flow rate using the rating curve described in Section S3.2. The left panel covers 29 June – 7 July and the right panel 17 – 19 August, 2011.*

The pressure probe at L57 was installed from days 220 – 224 (8 – 12 August, 2011), and was located at the outflow from a lake approximately 200 m upstream from the moulin. Only one salt dilution was possible, which coincided with the trace at L57 on 12 August. This yielded a flow rate of 3.2 m^3 s^{-1} at 21:12 hrs local time, when the water depth in the stream was 0.32 m (Fig. S3.4). Given the timing of this measurement (shortly after the diurnal peak) we estimate the flow rate into L57 was approximately 50-70% of that feeding L41 during our late-season tracing period. The flow into L57 also followed the characteristic diurnal pattern with a peak at approximately 18:00-20:00 hrs.

Despite covering a very limited period, these flow rate measurements indicate the characteristics of the surface input of water driving the englacial and subglacial drainage system, showing that flow rates can vary by up to an order of magnitude over one diurnal cycle.

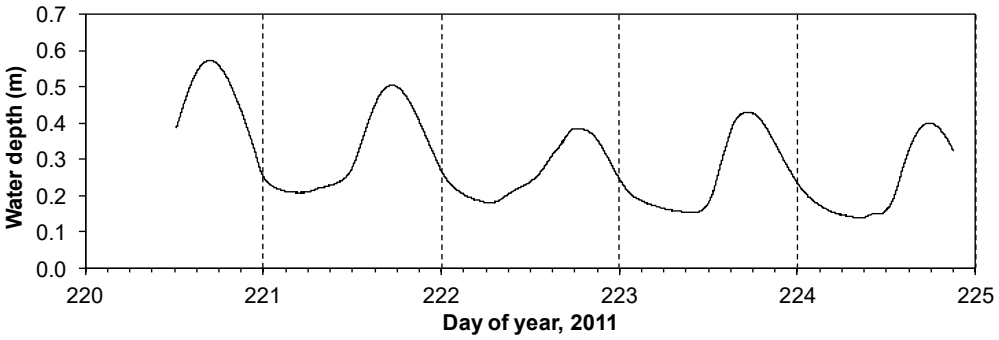

Figure S3.4: *Water depth in the stream feeding Moulin L57 during days 220 – 224 (8 – 12 August) 2011. The single SF_6 trace of L57 was injected at the end of this period (20:30 hrs, 12 August).*

S4. CHANNEL CREEP CLOSURE MODEL

Here we use Schoof's[14] Equation 1, which describes the rate of subglacial channel expansion in full water-filled channels with semi-circular cross section. This equation considers three processes: expansion due to heat dissipation by the water flow, expansion due to basal sliding (opening of

cavities in the lee of bedrock steps) and closure due to viscous creep of the ice. Since the sliding component opens cavities which are isolated and likely to be oriented perpendicular to ice flow (and therefore perpendicular to the general direction of water flow), we could treat cavity opening as a storage process rather than channel process. This might be reasonable even with rapid sliding: the resulting cavities oriented normal to ice flow must still be linked by channels parallel to ice flow, so the opening of channels remains as the rate-limiting process. Therefore we can omit the sliding term, and use the following reduced equation:

$$\frac{dS}{dt} = c_1 Q\Psi - 2An^{-n}N^n S \qquad \text{[S4.1]}$$

where S is channel cross-section area, c_1 is a constant, Q is channel water flux, Ψ is hydraulic potential, A is the rate factor in Glen's flow law, n is the exponent in Glen's flow law, $N = \rho_i g H - p_w$ is effective pressure, ρ_i is ice density, p_w is water pressure in the channel, H is ice thickness and g is acceleration due to gravity. The first term on the RHS is the expansion due to viscous heat dissipation and the second term is the creep closure rate.

If we first consider the case of unpressurised channels with little water flow, such as may be the case during the winter if the channels empty, the Q term in Eq. S4.1 can be neglected. We can also set $N = \rho_i g H$ and the initial channel cross section $S = S_0$. Then Eq. (4.1) can then be solved to give S:

$$S / S_0 = \exp[-2An^{-n}(\rho_i g H)^n t]. \qquad \text{[S4.2]}$$

Using Eq. S4.2 to calculate the time required for channel radius to shrink to a tenth of its original radius (i.e., when $S/S_0 = 1/100$ or $R/R_0 = 1/10$), we find that channels are likely to close very rapidly during the winter (Fig 2c in the main paper): after 8 months (equivalent to the period of low melt input from mid September to mid May), channel cross section areas will decrease by 99% under ice thicker than 90 m. These figures are consistent with the tracing results from Site L7 (the lowest site with early season data), where the ice thickness is ~400 m and the drainage system was inefficient at the start of the melt season.

In the more general case of pressurised channels and when $Q > 0$, the hydraulic potential Ψ driving the water flow in direction s is[14]:

$$\Psi = -\rho_w g \frac{\mathrm{d}b}{\mathrm{d}s} - \frac{\mathrm{d}p_w}{\mathrm{d}s}. \qquad [S4.3]$$

Over long length scales, limited radio echo sounding data indicate that the bed of the Leverett catchment is relatively flat when compared with the surface slope[15], so for present purposes we use the approximation $\mathrm{d}b/\mathrm{d}s = 0$. Applying this to Eq. (4.3) and substituting $p_w = p_i - N$ gives

$$\Psi = \frac{\mathrm{d}N}{\mathrm{d}s} - \frac{\mathrm{d}p_i}{\mathrm{d}s} \qquad [S4.4]$$

which is equivalent to Schoof's[14] Eq. 4 with $\mathrm{d}b/\mathrm{d}s = 0$. Calculating the time evolution of these quantities for a real catchment requires a detailed hydrological model beyond the scope of this study. However, our aim here is only to obtain an estimate of channel behaviour, so instead we specify p_w as a fraction β of the ice overburden pressure p_i (i.e., $p_w = \beta p_i = \beta \rho_i g H$). Now, Ψ can be expressed more conveniently in terms of the surface slope, which is a known quantity in the Leverett catchment:

$$\Psi = -\beta \rho_i g \frac{\mathrm{d}H}{\mathrm{d}s}. \qquad [S4.5]$$

Returning again to Schoof's model[14], the water flux Q is calculated using the Darcy-Weisbach law for turbulent water flow:

$$Q = (2/\pi)^{1/4}[(\pi + 2)/\rho_w f]^{1/2} S^{\alpha} |\Psi|^{-1/2} \Psi \qquad [S4.6]$$

with $\alpha = 5/4$ and $f = 0.1$. The factor $(\pi + 2)$ arises from the cross section perimeter length under the assumption of full, semicircular channels. Substituting $c_1 = 1/(\rho_i L)$ and putting Eqs. S4.5 and S4.6 into Eq. S4.1 yields:

$$\frac{dS}{dt} = k_1 S^{\alpha} - k_2 S \qquad [S4.7]$$

where

$$k_1 = \left(\frac{2}{\pi}\right)^{\frac{1}{4}}\left(\frac{\pi+2}{\rho_w f}\right)^{\frac{1}{2}}\left(\frac{1}{L\rho_i}\right)\left|\beta\rho_i g\frac{\mathrm{d}H}{\mathrm{d}s}\right|^{\frac{3}{2}} \geq 0;$$

$$k_2 = 2An^{-n}\left[(1-\beta)\rho_i gH\right]^n \geq 0. \qquad \text{[S4.8]}$$

Fixed points of Eq. S4.7 (when S remains constant with time) occur at $S = 0$ and at $S = S^* = (k_2/k_1)^{1/(\alpha-1)}$. $S = 0$ is a stable fixed point, since dS/dt for positive S very close to $S = 0$ is approximately $-k_2 S < 0$ when $\alpha > 1$. S^* must have the opposite stability to $S = 0$ if there are exactly 2 fixed points. Eq. S4.7 therefore predicts that channels greater than a critical size S^* grow, while those smaller than that critical size will shrink. In the end-member cases: as $\beta \rightarrow 0$, $S^* \rightarrow \infty$ (as water pressure drops to zero, channels of all size will shrink) and as $\beta \rightarrow 1$, $S^* \rightarrow 0$ (as floatation pressure is reached, channels of all size will grow).

Variations in R^* with β (Fig. S4.1) show the typical water pressures required to reach the unstable region ($R > R^*$) where channelised flow develops (in the plot, this is to the right of the curve). Ice geometry (thickness and surface slope) was estimated for the Leverett catchment using surface and bed DEMs[15,16]. Not surprisingly, only moderate water pressures are required at 1 km where the ice is shallow, while very high pressures (approaching floatation) are required for channel growth under deeper ice upstream.

The assumption of full, ice-walled semi-circular channels is a poor assumption in our case, since (a) the channel is at the bed, so any heat transfer to the base of the channel is dissipated into the substrate rather than being used locally for channel wall melting; (b) the channels may not always be full; and (c) the value of f for ice is much smaller than that for the channel base (rock or sediment). Consequently, the relatively rough base of the channel will reduce Q for a given S and β, and will sink a disproportionately large share of the turbulent heat relative to its contact area. This heat would presumably be used for basal melt over a region that is relatively large compared with that of the channel. To account for the different friction values of ice walls and bed material we use

the friction factors f_i, f_b which have fractional contributions to the wetted perimeter of $\pi/(2+\pi) \approx 0.61$ and $2/(2+\pi) \approx 0.39$, respectively. The ice walled area is therefore about 61% of the total channel surface area. We are still assuming channels are full, which retardation calculations from our tracing observations, as well as a borehole pressure record[17], suggest is valid everywhere except near the margin (sites below L7). Eq. (S4.6) for water flux now becomes

$$Q = (2/\pi)^{1/4}[\pi/f_i + 2/f_b]^{1/2}\rho_w^{-1/2}S^{\alpha}|\Psi|^{-1/2}\Psi \qquad [S4.9]$$

and the rate of wall melting is reduced in proportion to the fraction of the channel surface that is ice, so that $c_1 = \pi f_i/[(\rho_i L)(2f_b + \pi f_i)]$. This increases R^* relative to that obtained using Schoof's (2010) purely ice-walled channels (Fig S4.1). The most notable result from this calculation, with respect to maintaining channelised flow, is the very marked change between L1 (where very little water pressure is required to maintain channels) and the higher sites (L7 and upwards, where water pressures exceeding 70-95% of overburden are required)

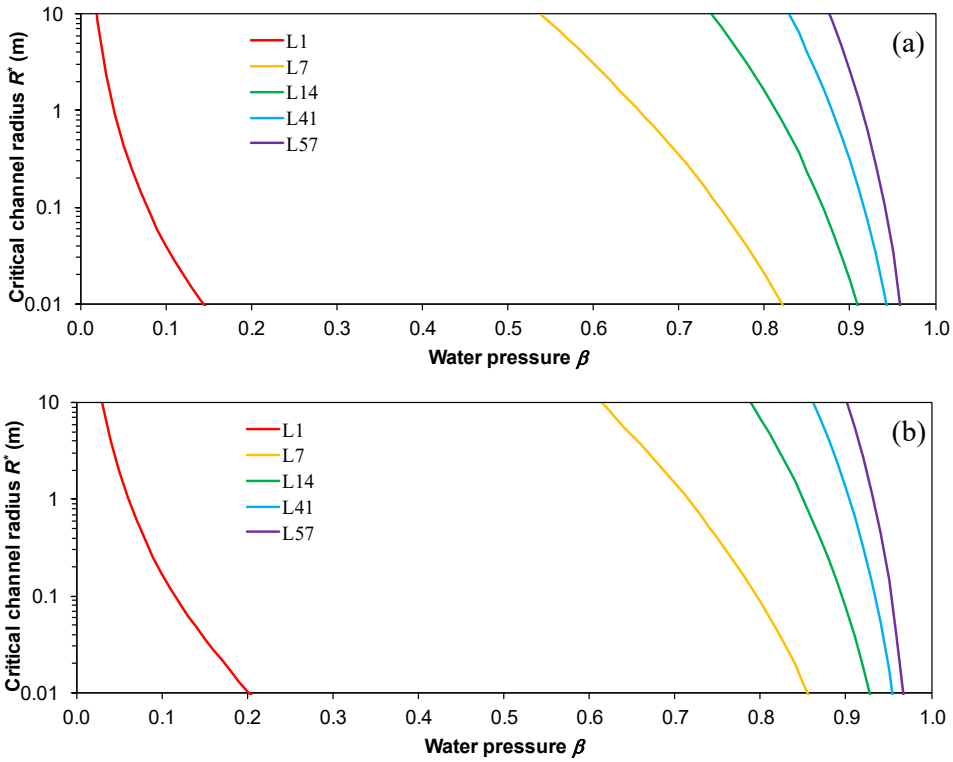

Fig. S4.1: *Variation in critical radius R^* with channel pressurisation β, calculated using estimated values of H and dH/ds for locations at increasing distances from the terminus. Part (a): semicircular channels with ice walls and floor, using parameters suggested by Schoof[7]); part (b) is the same as (a) but with a sediment-based channel.*

Next we estimate the time scale for channel growth. Eq. S4.7 is separable and can be solved to obtain S as a function of time as follows.

$$\mathrm{d}t = \frac{\mathrm{d}S}{k_1 S^{\alpha} - k_2 S} \qquad \text{[S4.10]}$$

Substituting $S^{*(\alpha-1)} = k_2/k_1$, then integrating, we get:

$$\int \mathrm{d}t = \frac{1}{k_1}\int \frac{\mathrm{d}S}{S\left(S^{(\alpha-1)} - S^{*(\alpha-1)}\right)}. \qquad \text{[S4.11]}$$

Expanding the RHS of S4.11 using partial fractions and setting $\gamma = a - 1 = ¼$ gives:

$$k_1 \int \mathrm{d}t = \frac{1}{S^{*\gamma}}\int \frac{S^{(\gamma-1)}}{S^{\gamma} - S^{*\gamma}}\mathrm{d}S - \frac{1}{S^{*\gamma}}\int \frac{\mathrm{d}S}{S} \qquad \text{[S4.12]}$$

which, using the substitution $u = S^{\gamma} - S^{*\gamma}$ in the first integral on the RHS, has the solution:

$$S^{*\gamma} k_1 \left(t - t_0\right) = \frac{\ln\left|S^{\gamma} - S^{*\gamma}\right|}{\gamma} - \ln\left|S\right| \qquad \text{[S4.13]}$$

where t_0 is a constant of integration. Providing $S > 0$ and $\alpha > 1$, we then have two equations in S:

$$\gamma S^{*\gamma} k_1 \left(t - t_0\right) = \ln\left(S^{*\gamma} - S^{\gamma}\right) - \gamma \ln S; \quad S < S^{*} \qquad \text{[S4.14a]}$$

$$\gamma S^{*\gamma} k_1 \left(t - t_0\right) = \ln\left(S^{\gamma} - S^{*\gamma}\right) - \gamma \ln S; \quad S > S^{*}. \qquad \text{[S4.14b]}$$

Rearranging,

$$-\exp\left[\gamma S^{*\gamma} k_1 \left(t - t_0\right)\right] = 1 - \left(\frac{S^{*}}{S}\right)^{\gamma}; \quad S < S^{*} \qquad \text{[S4.15a]}$$

$$\exp\left[\gamma S^{*\gamma} k_1 \left(t - t_0\right)\right] = 1 - \left(\frac{S^{*}}{S}\right)^{\gamma}; \quad S > S^{*}. \qquad \text{[S4.15b]}$$

Using the initial condition $S = S_0$ at $t = 0$ gives, for both Eqs.S4.15a and S4.15b after some manipulation:

$$S = S^{*}\left[1 + \eta \exp\left(\gamma S^{*\gamma} k_1 t\right)\right]^{-\frac{1}{\gamma}} \qquad \text{[S4.16]}$$

where $\eta = (S^*/S_0)^\gamma - 1$. For $S_0 < S^*$, Eq. S4.16 shows S decays to zero, while for $S_0 > S^*$, S increases and becomes infinite in a finite time $t = (\gamma S^{*\gamma} k_1)^{-1} \ln(-\eta^{-1})$. In a real system this unbounded channel growth would be limited by the available water supply. Plotting Eq. S4.16 for Sites L7, L14, L41 and L57 shows the marked difference in calculated channel growth rates between the sites (Fig S4.2). For example, with the water pressure close to overburden ($\beta = 1$), doubling the radius of a small channel (initial channel radius 0.25 m) would take 10 days at L7 compared with 23 days at L41 and 28 days at L57. Evidence for persistently high water pressure, as is assumed here, is provided by a water pressure record in a borehole adjacent to a moulin located low in the catchment (between L7 and L14)[17], which shows water pressure remained close to overburden in ice ~600 m thick well into the 2010 melt season. The field observations and model results are therefore consistent in suggesting the drainage system can and does become channelised through the melt season at least as far as L41, but that these channels remain at high pressure upglacier of a narrow (< 7 km wide) marginal zone.

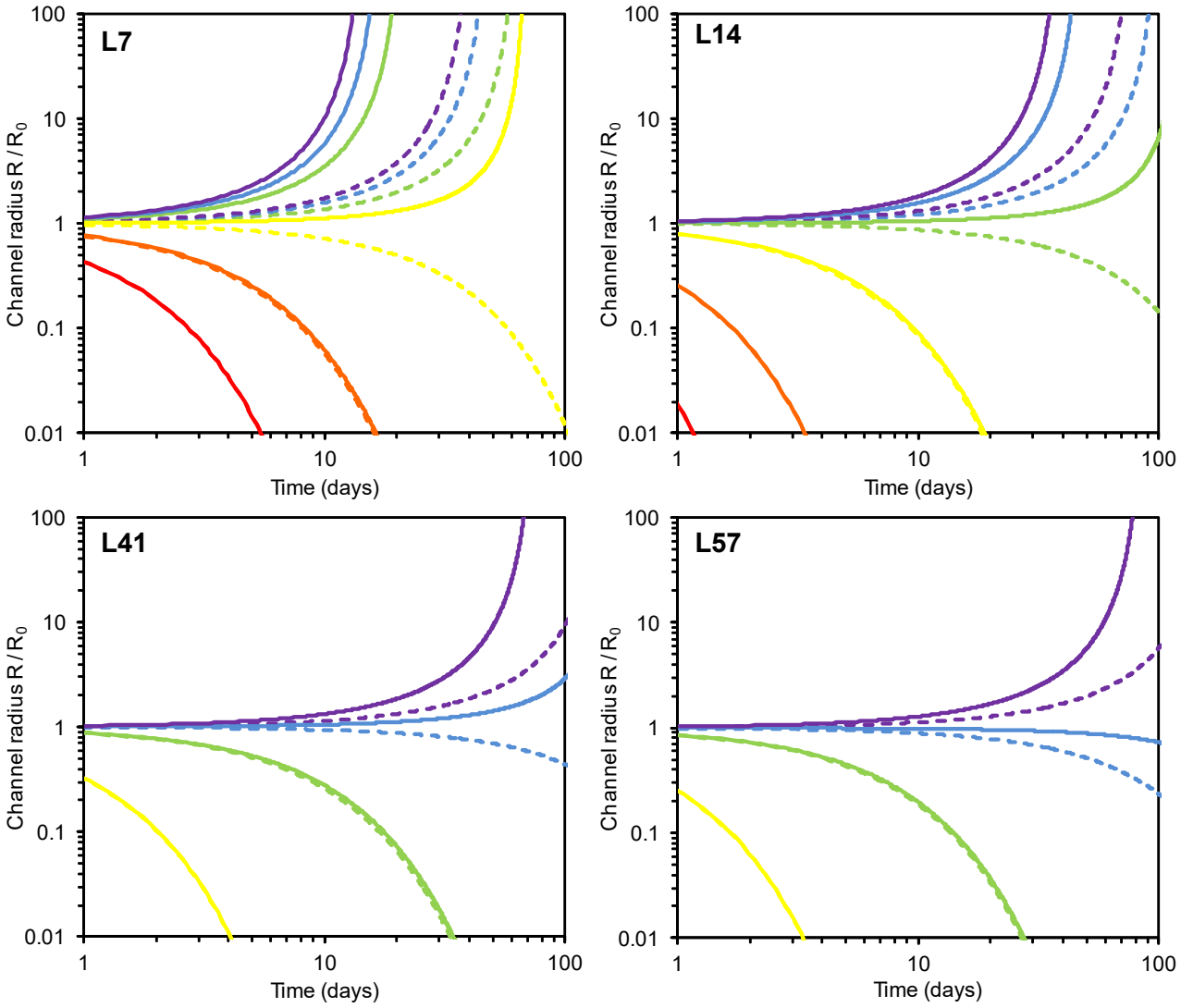

Figure S4.2: *Channel growth at sites L7, L14, L41 and L57. Initial channel size is R_0 is 0.25 m (dashes) and 1 m (solid lines). Water pressure β is 0 (red), 0.3 (orange), 0.6 (yellow), 0.8 (green), 0.9 (blue) and 1.0 (purple).Water flux was calculated for sediment-floored channels (Eq. S4.8) with $f_b = 0.3$. As β decreases, the solid and dashed lines for the large and small channels become closer, because the channel evolution is increasingly dominated by the creep closure term which is independent of channel radius.*

An important process that is not included in the present model, nor in Schoof's[14] more detailed original version, is ice-bed separation ('hydraulic jacking') during periods of very rapid water input. This is distinct from 'cavitation', which occurs when sliding is sufficiently fast to leave cavities in the lee of bedrock obstacles and steps[18]. Ice-bed separation is observed at the ice surface as rapid uplift, and is a characteristic of lake drainage events observed in the ablation zone of the ice sheet when large (order 10^7 m^3) supraglacial lakes empty over a few hours[19,20]. These events are associated with transient surface uplift of several tens of centimetres. Lesser amounts of uplift have

also been observed during periods of high discharge in rivers feeding moulins[13]. In either case the ice-bed separation is thought to be caused by the drainage system being insufficiently developed to evacuate such high melt inputs[13,19,20]. Clearly, extensive ice-bed separation of these magnitudes would be equivalent to the formation of numerous very broad but low channels capable of rapidly transporting large volumes of melt water. This process would allow a much faster response of the drainage system to peak supraglacial melt inputs than the times estimated in the channel model above, but is likely to be limited to extreme cases where high melt inputs are sufficiently sustained to maintain the high subglacial water pressures required for widespread ice-bed separation. Nevertheless, such events may be important in initialising channel formation and should be considered in future drainage system models.

References

1. J.L. Bullister, D.P. Wisegarver and F.A. Menzia. The solubility of sulfur hexafluoride in water and seawater, *Deep Sea Research Part I*, **49**, 175–187, doi:10.1016/S0967-0637(01)00051-6 (2002).
2. Turner Designs (2012). http://www.turnerdesigns.com/products/submersible/cyclops-7.
3. S.Z. Seaberg, J.Z. Seaberg, R. LeB. Hooke and D. Wieberg. Character of the englacial and subglacial drainage system in the lower part of the ablation area of Storglaciären, Sweden, as revealed by dye-trace studies. *Journal of Glaciology* **34**, 217-227 (1988).
4. P. Jansson. Dynamics and hydrology of a small polythermal valley glacier. *Geografiska Annaler* **78A**, 171-180 (1996).
5. P.W. Nienow, M. Sharp and I.C. Willis. Seasonal changes in the morphology of the subglacial drainage system, Haut Glacier d'Arolla, Switzerland. *Earth Surface Processes and Landforms* **23**, 825-843 (1998).
6. R.G. Bingham, P.W. Nienow, M.J. Sharp and S. Boon. Subglacial drainage processes at a High Arctic polythermal valley glacier. *Journal of Glaciology* **51**, 15-24 (2005).
7. E. Busenberg and L.N. Plummer. A rapid method for the measurement of sulfur hexafluoride (SF_6), trifluoromethyl sulfur pentafluoride (SF_5CF_3), and Halon 1211 (CF_2ClBr) in hydrologic tracer studies. *Geochemistry Geophysics Geosystems* **11,** Q11001, doi:10.1029/2010GC003312 (2010).
8. R. Wanninkhof, J.R. Ledwell and A.J. Watson. Analysis of sulfur hexafluoride in seawater. *Journal of Geophysical Research* **96**, 8733-8740 (1991).
9. K.S. Dillon, D.R. Corbett, J.P. Chanton, W.C. Burnett and L. Kump. Bimodal transport of a waste water plume injected into saline groundwater of the Florida Keys. *Groundwater* **38** 624-634 (2000).
10. V.M. Vulava, E.B. Perry, C.S. Romanek and J.C. Seaman. Dissolved gases as partitioning tracers for determination of hydrogeological parameters. *Environmental Science and Technology* 36, 254-262 doi:10.1021/es0107024 (2002).
11. J.F. Clark, P. Schlosser, M. Stute and H.J. Simpson. SF_6–^{3}He tracer release experiment: A new method of determining longitudinal dispersion coefficients in large rivers. *Environmental Science and Technology* **30**, 1527-1532 (1996).

12. D.T. Ho, P. Schlosser and T. Caplow. Determining longitudinal dispersion coefficient and net advection in the tidal Hudson River with a large-scale, high-resolution SF_6 tracer release. *Environmental Science and Technology* **36**, 3234-3241 doi:10.1021/es015814 (2002).
13. I.D. Bartholomew, P. Nienow, D. Mair, A. Hubbard, M.A. King and A. Sole. Seasonal evolution of subglacial drainage and acceleration in a Greenland outlet glacier. *Nature Geoscience* **3**, 408-411 (2010).
14. C. Schoof. Ice-sheet acceleration driven by melt supply variability. *Nature* **468**, 803-806 (2010).
15. C. Allen. *IceBridge MCoRDS L2 Ice Thickness* [2010, 2011]. Boulder, Colorado, USA: NASA DAAC at the National Snow and Ice Data Center. http://nsidc.org/data/irmcr2.html (2010, updated current year).
16. S. Palmer, A. Shepherd, P. Nienow and I. Joughin. Seasonal speedup of the Greenland Ice Sheet linked to routing of surface water. *Earth and Planetary Science Letters* **302**, 423-428 (2011).
17. C.J.P.P. Smeets, W. Boot, A. Hubbard, R. Pettersson, F. Wilhelms, M.R. van den Broeke and R.S.W. van de Wal. A wireless subglacial probe for deep ice applications. *Journal of Glaciology* **58,** 841-848 (2012).
18. L. Lliboutry. General theory of cavitation and sliding of temperate glaciers. *Journal of Glaciology* **7**, 21-58 (1968).
19. S.B. Das, I. Joughin, M.D. Behn, I.M. Howat, M.A. King, D. Lizarralde and M.P. Bhatia. Fracture propagation to the base of the Greenland Ice Sheet during supraglacial lake drainage. *Science* **320**, 778-781, doi:10.1126/science.1153360 (2008).
20. S.H. Doyle, A.L. Hubbard, C.F. Dow, G.A. Jones, A. Fitzpatrick, A. Gusmeroli, B. Kulessa, K. Lindback, R. Pettersson and J.E. Box. Ice tectonics during the rapid tapping of a supraglacial lake on the Greenland Ice Sheet. *The Cryosphere Discussions* **6**, 3863-3889 (2012).